11

Interferometric Measurement in Shock Tube Experiments

Masanori Ota, Shinsuke Udagawa, Tatsuro Inage and Kazuo Maeno
Graduate School of Engineering, Chiba University
Japan

1. Introduction

This chapter describes applications of interferometry to the shock tube experiments. The first topic is Laser Interferometric Computed Tomography (LICT) technique to realize the three-dimensional (3D) density measurement of high-speed and unsteady flow field behind shock waves discharging from nozzles. The second topic is measurement of propagating shock wave in micro-scale shock tube by interferometic approach. Micro-scale shock tube is being researched in several fields of science recently and micro-scale shock wave has possibilities of applications for various fields - medical, engineering, …etc. Clarifying the characteristics of micro-scale shock tube to generate the micro-scale shock wave is very important step for the application.

2. Laser Interferometric Computed Tomography (LICT) technique

The purpose of this investigation is to develop Laser Interferometric Computed Tomography (LICT) technique to observe high-speed, unsteady and three-dimensional (3-D) flow field that includes shock wave, and to clarify 3-D flow phenomena induced by shock waves. In our previous study, 3-D complex flow discharged from a square nozzle and a pair of circular nozzles was measured by LICT tchnique (Maeno et al., 2005; Ota et al., 2005; Honma et al., 2003a, 2003b). The shock Mach number at the exits of the nozzles were both higher and lower than 2.0. As a result, various phenomena of 3-D flow field were clarified by several imaging technique such as pseudo-color images, pseudo-schlieren images by pseudo-schlieren technique, 3-D isopycnic images, etc. Three-dimensional and complex flow phenomena behind shock wave were elucidated precisely and reported (Honma et al., 2003a, Maeno et al., 2005), therefore this chapter reports measurement results mainly.

2.1 Experimental apparatus

Diaphragmless shock tube is employed to produce a shock wave with good reproducibility. Figure 1 illustrates a schematic diagram of LICT experimental apparatus and observation system. The observation system consists of a CCD camera, a Mach-Zehnder interferometer, a pulsed nitrogen laser, a delay/pulse generator, an oscilloscope, and a personal computer.

The shock wave is generated by a diaphragmless shock tube driver in the low-pressure tube of 3.1 meters in length, and its inner cross section is 40 mm x 40 mm square. A rotating plug

is installed at the end of the low-pressure tube. The duct is open to the low-pressure test section.

To obtain the 3-D image of flow field, we need multidirectional projection data for a reproducible flow. A set of experiments has been performed for several rotation angles at the combination of fixed initial gas conditions for the high-pressure chamber and the low-pressure tube. Figure 2 shows coordinate system of rotating plug relative to the light pass s. We define x and y axes as shown in Fig.2, where these axes rotate with rotating plug. The z is central axis of rotating plug and is perpendicular to x and y axes. Rotation angle θ can be controlled from outside the shock tube with introduced rotation driving equipment. The experiment is performed for 19 rotation angles between 0 degree and 90 degrees at five-degree intervals while the light path s is fixed, taking benefit of the two-axis symmetrical characteristics of the flow field. The 3-D density distribution is reconstructed from a set of projection data for the same M_i and z_s. The Mach number of the incident shock wave M_i is calculated by pressure jump across the shock wave at the pressure transducer installed at 61mm ahead of the inlet of the rotating plug as shown in Fig. 3. In this paper M_i is fixed to 2.0. Mach-Zehnder interferometer is conventional one as shown in Fig. 4

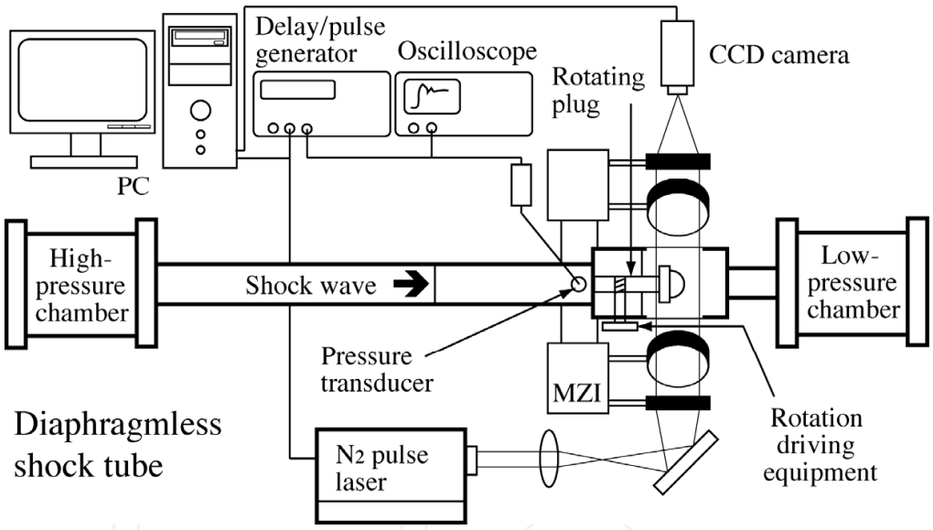

Fig. 1. Schematic diagram of experimental apparatus.

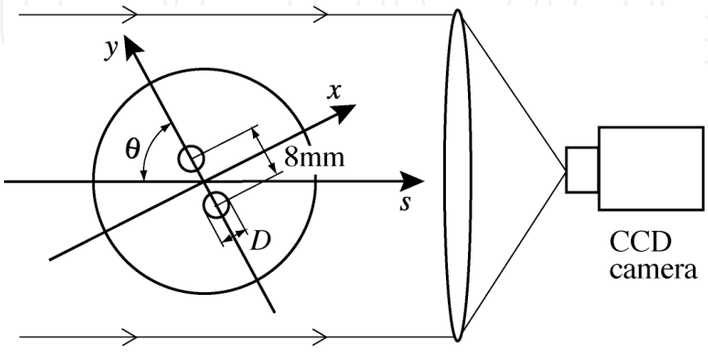

Fig. 2. Coordinate system of the rotating plug.

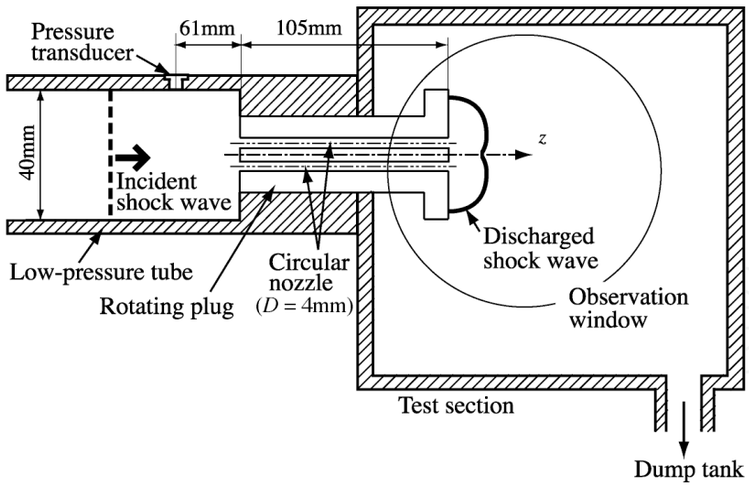

Fig. 3. Layout of rotating plug.

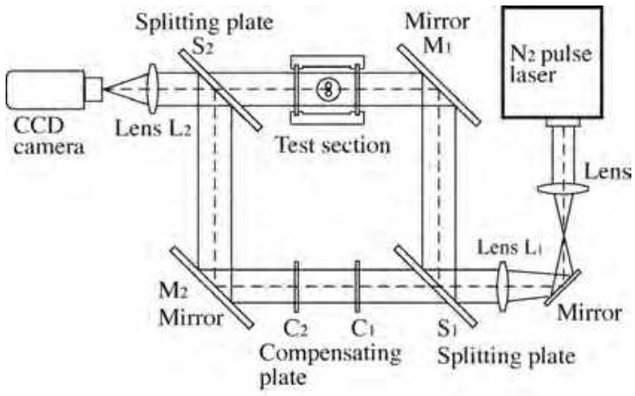

Fig. 4. Mach-Zehnder interferometer.

2.2 Projection data for LICT measurement

Figure 5 shows a finite-fringe interferogram at rotation angle $\theta = 90^{o}$ taken by CCD camera with Mach-Zehnder interferometer illustrated in Fig. 4. To obtain higher accuracy, we have taken interferogram of the lower half part of whole flow field, taking benefit of the two-axis symmetrical characteristics of the flow field. Thick blanked line indicates the central axis of rotating plug, and thin blanked line indicates the central axis of circular nozzles. The distance between these two central axes is 4mm. In this figure z_s is a frontal position of the primary shock wave, D is a diameter of circular nozzle (4mm), and z_s/D is the normalized frontal position of the primary shock wave. In this paper we discuss the case data of z_s/D = 2.50.

In LICT measurement, three-dimensional density distribution is reconstructed from multidirectional projection data. Projection data are calculated from Eq. 1, where ΔH is displacement of fringe pattern, Δh is interval of fringe pattern, λ is wavelength of observation light, and K is Gladstone-Dale index. ΔH and Δh in the right hand side in Eq. 1 are calculated from finite-fringe interferogram as shown in Fig. 5. Firstly, we calculate Δh at A section of no flow area. Secondly, we calculate ΔH from displacement of fringe pattern

comparing with A section. We obtain the integrated value of density change along the light pass from Eq. 1. Figure 6 shows the calculated projection data at B section of rotation angle $\theta = 90^{o}$. The horizontal axis indicates the vertical position of the finite-fringe image shown in Fig. 5, the origin of the coordinates is located in left top position of this image. The vertical axis of Fig.6 indicates the calculated integrated value of density change and its value is normalized with the initial density (ρ_0) at A section. We repeat this process for all projection angles at one cross section to obtain the multidirectional projection data at one cross section. Then 2-D density distribution is reconstructed from these projection data with appropriate reconstruction algorithm. Finally, 3-D density distribution is obtained as collection of reconstructed 2-D density distribution.

$$\int_0^d \{\rho(x,y,z) - \rho_0\}\, ds = \frac{\Delta H}{\Delta h}\frac{\lambda}{K} \tag{1}$$

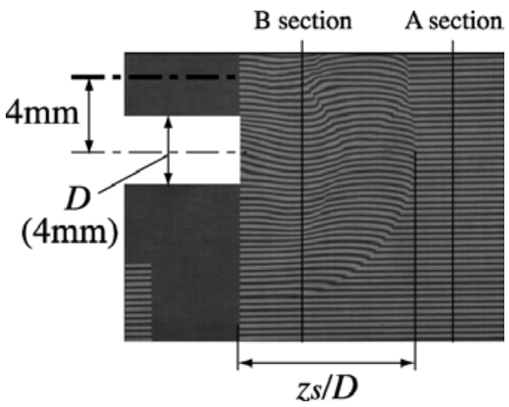

Fig. 5. Finite-fringe interferogram at rotation angle $\theta = 90^{o}$.

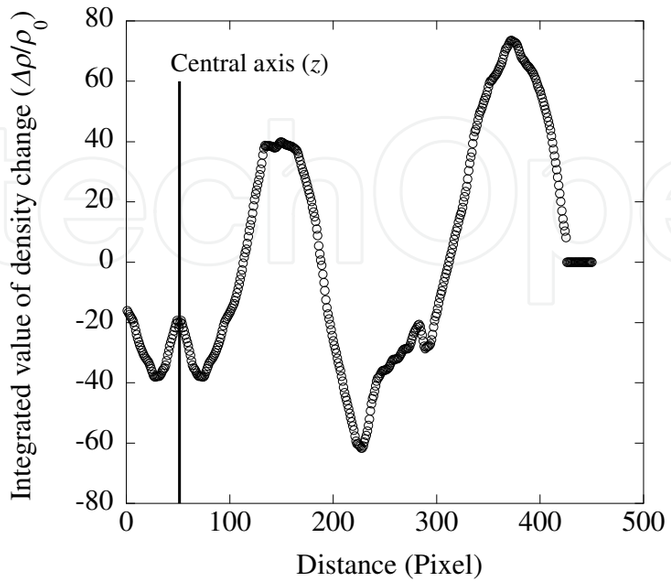

Fig. 6. Calculated projection data at B section in Fig. 5.

2.3 Results and discussion

Figure 7 shows the pseudo-color images of normalized density distribution and the pseudo-schlieren images indicating the magnitude of the density gradient $\nabla|\rho/\rho_0|$ at y-z cross-section. In pseudo-color image the density level is shown in visible-light color spectrum. The black line with white blank indicates the rotating plug with circular nozzles, where white blank corresponds to a pair of circular nozzles. The experimental condition is M_i = 2.0, z_s/D = 2.50 as mentioned above. The smoothing filter is applied to the reconstructed 3-D density distribution with FBP algorithm before the calculation of the density gradient, for reducing the noise in the resultant pseudo-schlieren image. In pseudo-color image two vortex rings around the discharged flow from two circular open cylinders are illustrated. The primary shock wave (PSW), secondary shock wave (SSW), contact surface (CS1, CS2), and transmitted shock wave (TSW) are exhibited clearly in pseudo-schlieren image.

Pseudo-color image of normalized density distribution at x-y cross-section is shown in Fig. 8. Position of the x-y cross section is indicated with normalized distance z/D where z is the distance between the rotating plug's wall and the x-y cross section. In these images cross sectional shape of PSW, TSW and two vortex rings around the discharged flow is exhibited. Figure 9 shows the pseudo-schlieren images at x-y cross-sections. In these images PSW, the shock-vortex interaction between TSW and vortex, shock-shock interaction between TSW and PSW are exhibited clearly.

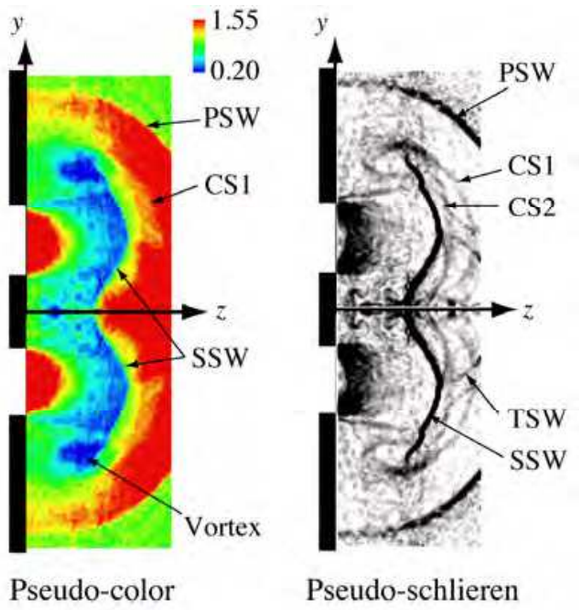

Fig. 7. Pseudo-color (left) and pseudo-schlieren (right) image at y-z cross-section.

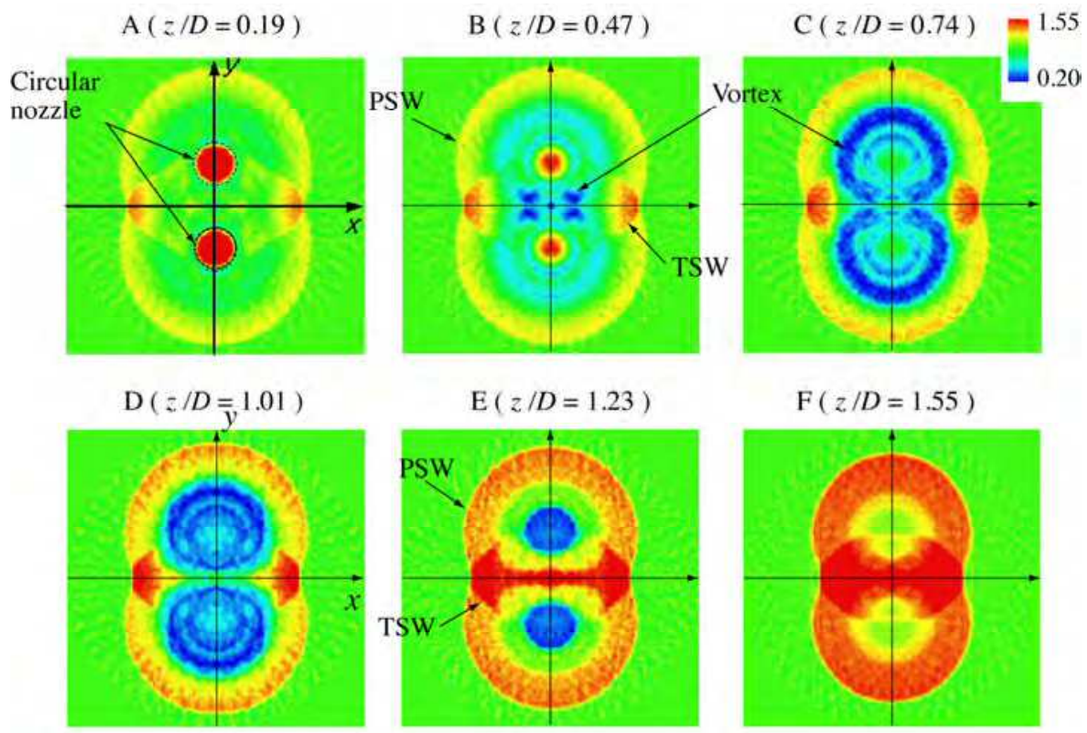

Fig. 8. Pseudo-color images of density distribution at *x*-*y* cross-sections.

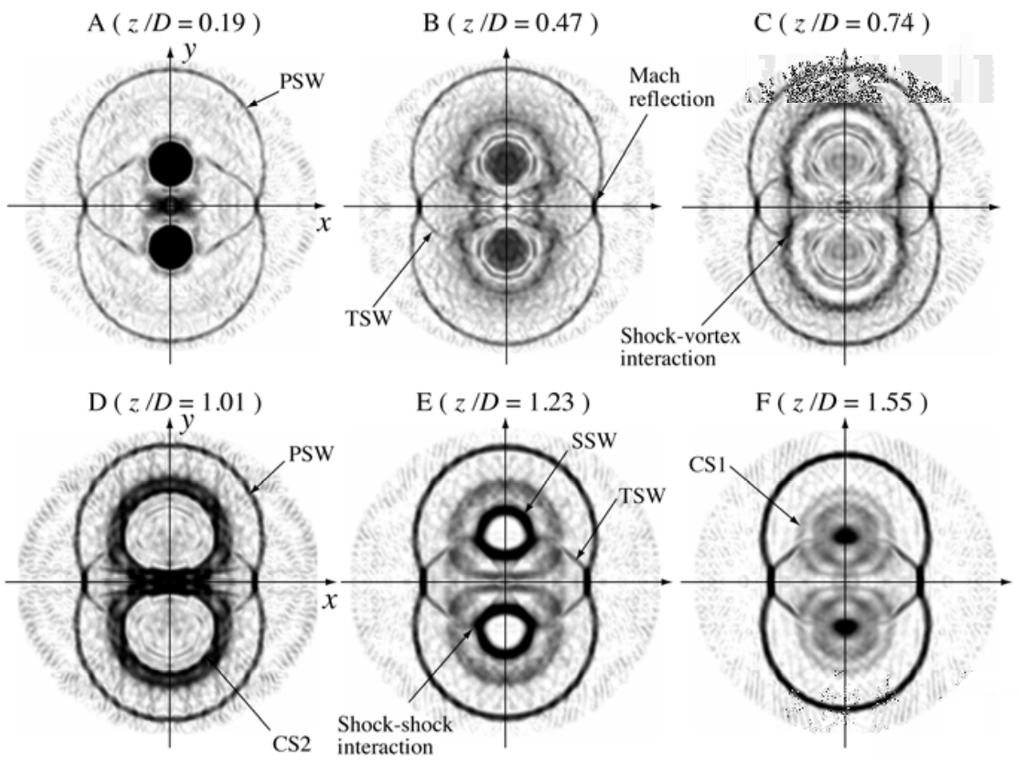

Fig. 9. Pseudo-schlieren images of density gradient ($\nabla|\rho / \rho_0|$) at *x*-*y* cross-sections.

3. LICT Measurement of flow field around the object

Three-dimensional observation of flow field around object will be important to apply CT measurement to more general case. Therefore LICT technique has been applied to the flow field around a circular cylinder as shown in Fig. 10. Diameter of a cylinder is 4mm, length 10mm and it was installed at intervals of 8mm from a cylindrical nozzle. In this case the problem is reconstruction has to be done from incomplete projection data. The object in the observation area blocks off the observation light for interferometry as shown in Fig. 11, the calculated projection data also contain the blank part which corresponds to the position of the circular cylinder as indicated in Fig. 12. This section describes the reconstruction of flow field around object with ART algorithm and results.

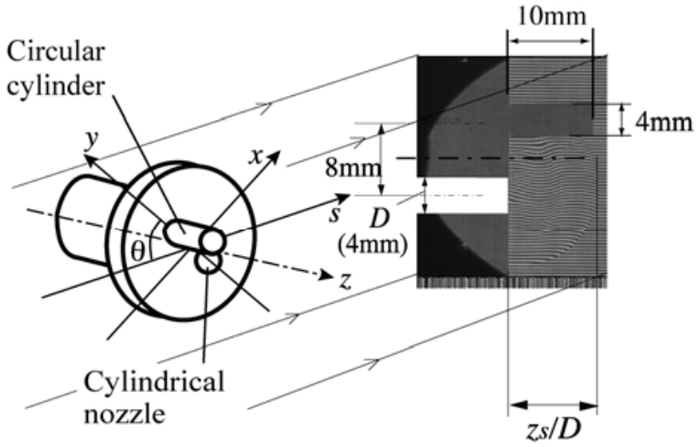

Fig. 10. Coordinate system of rotating plug and finite-fringe interferogram.

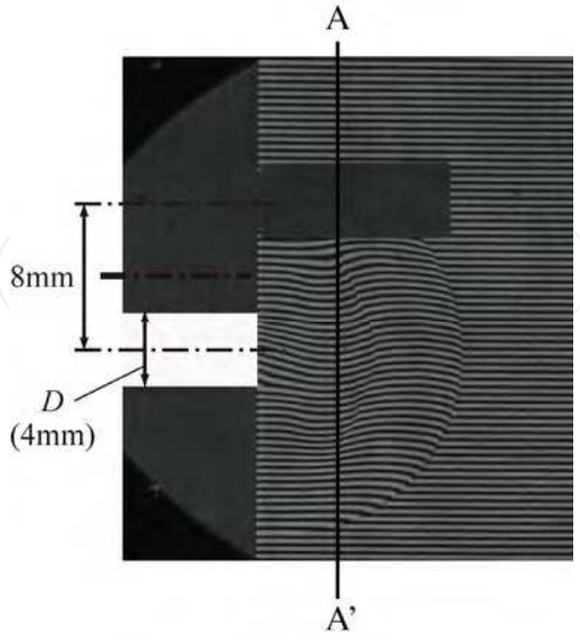

Fig. 11. Finite-fringe interferogram at rotation angle $\theta = 90^{o}$.

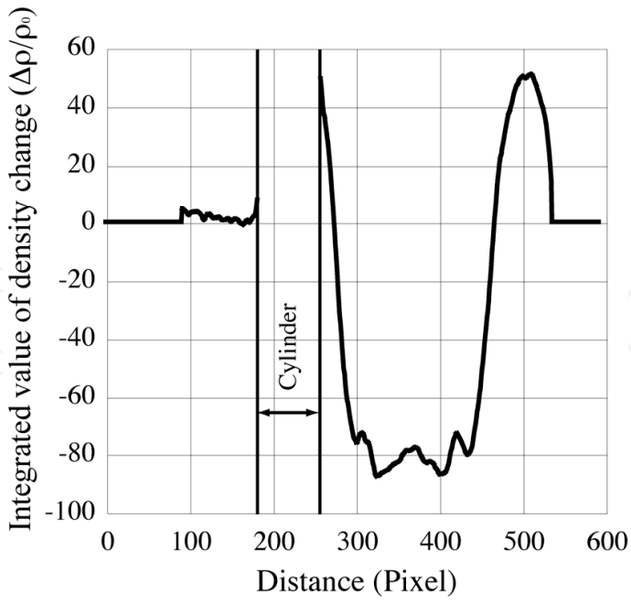

Fig. 12. Calculated projection data at A-A′ section in Fig. 11.

3.1 Reconstruction algorithm

In previous section, 3-D density distribution was reconstructed by FBP (Filtered Back Projection) with Shepp and Logan type filter (Shepp & Logan, 1974). FBP is the most common technique for the tomographic reconstruction. In this chapter the density distribution of unsteady flow field around a circular cylinder is reconstructed by ART (Algebraic Reconstruction Technique). This technique is one of the iterative reconstruction method and consists of assuming that the cross section consists of an array of unknowns, and then setting up algebraic equations for the unknowns in terms of the measured projection data (Kak & Slaney, 1988). ART is much simpler than FBP method which is the transform-based method and we have used in our previous study. For FBP a large number of projections is required for higher accuracy in reconstructed image, in the situation where it is not possible to obtain these projections the reconstructed image is suffer from many streaky noise. The reconstruction from incomplete projection data is more amenable to solution by ART. Figure 13 shows comparison between FBP and ART reconstruction. Left figure is pseudo-color image at the same plane illustrated in Fig. 7 and right figure is pseudo-schlieren image. Upper half image is reconstructed by FBP and lower half is by ART. In pseudo-color image, reconstructed density distribution by ART is clearer than FBP result. The smoothing filter is applied to the reconstructed density distribution before the calculation of density gradient for FBP result as mentioned above. On the other hand, no smoothing filter is applied for ART result however density gradient is captured distinctly. Figure 14 is comparison between FBP and ART illustrated by pseudo-color and pseudo-schlieren image at x-y cross section (normalized position z/D = 0.74). In pseudo-color image some radial noises from the center can be seen in FBP result (upper), however these noises are reduced in ART result (lower) drastically. Though no smoothing filter is applied, flow phenomena are clearly seen with ART result in pseudo-shclieren image. In our experiments density distribution is reconstructed from 19 projections that is based on our experiences.

Larger projection number will better to obtain higher accuracy, however it will cause inefficiency of experiments and data processing. Figure 13 and 14 show that ART is effective for reconstruction from incomplete projection data when LICT measurement is applied to the measurement of flow field around a circular cylinder. In this chapter blanked part in projection data where a circular cylinder is captured in projection plane does not contribute to reconstruction. Projection number is 19 rotation angles from 0° to 90° at 5° intervals as previous case.

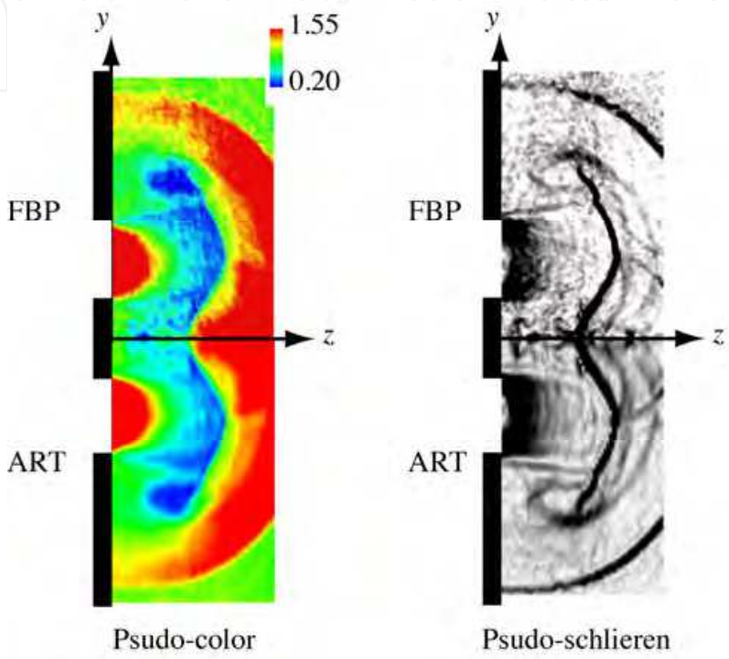

Fig. 13. Comparison between FBP and ART at *y*-*z* cross-section.

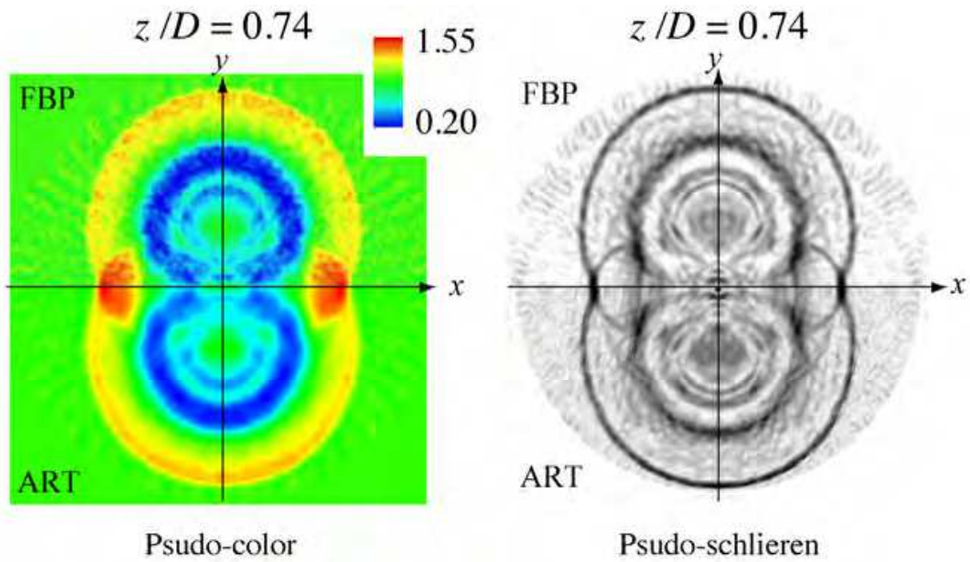

Fig. 14. Comparison between FBP and ART at *x*-*y* cross-section.

3.2 Results and discussion

The resultant image in *y-z* cross section is illustrated in Fig. 15. The left is pseudo-color image of normalized density distribution and right is pseudo-schlieren image. The vertical thick line with white blank indicates rotating plug's wall and white blank indicates a cylindrical nozzle. The position of a circular cylinder is indicated with two horizontal blanked lines. The vortex around discharging flow from a cylindrical nozzle is identified in pseudo-color image and primary shock wave (PSW), secondary shock wave (SSW), contact surface (CS) and reflected shock wave (RSW) from circular cylinder is clearly seen in pseudo-schlieren image.

Figure 16 illustrates pseudo-color images of normalized density distribution in *x-y* cross section. Six cross sections (position A~F) that are parallel to rotating plug's wall are indicated. The normalized position of cross section (*z/D*) is shown at upper side of each image. The position of a circular cylinder is indicated with blanked circle. In position A~C, the cross sectional shape of vortex around the discharging flow from a cylindrical nozzle is captured. The reflected shock wave (RSW) from circular cylinder is seen in position D~F. Four slanting noise from a circular cylinder is appeared in position E and F, this is influence of reconstruction from incomplete projection data.

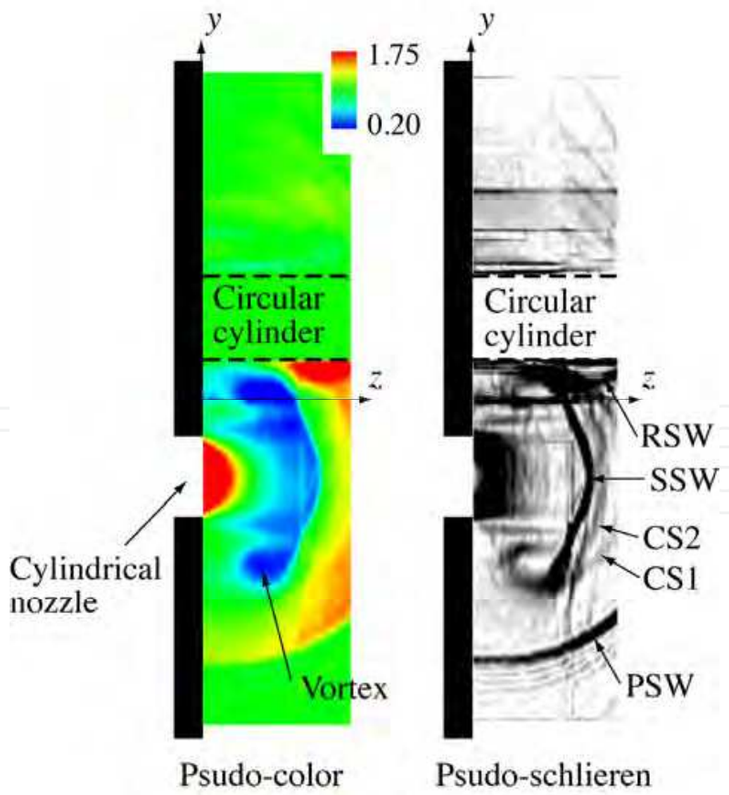

Fig. 15. Pseudo-color (left) and pseudo-schlieren (right) image at *y-z* cross-section.

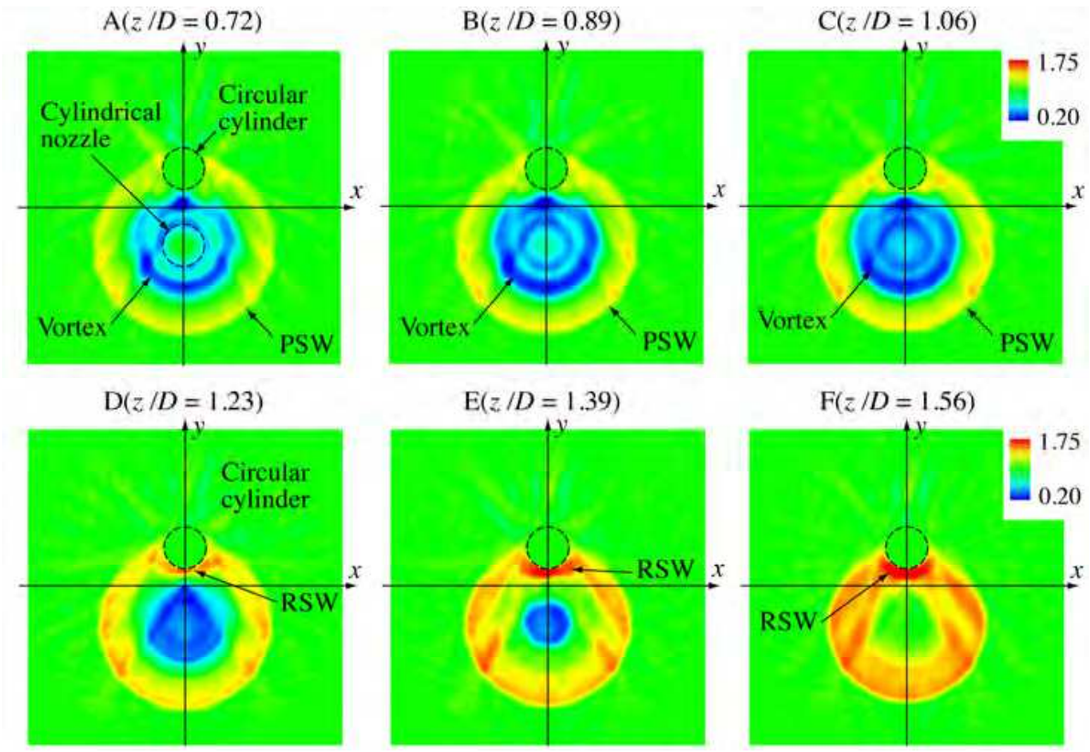

Fig. 16. Pseudo-color images of density distribution at *x*-*y* cross-sections.

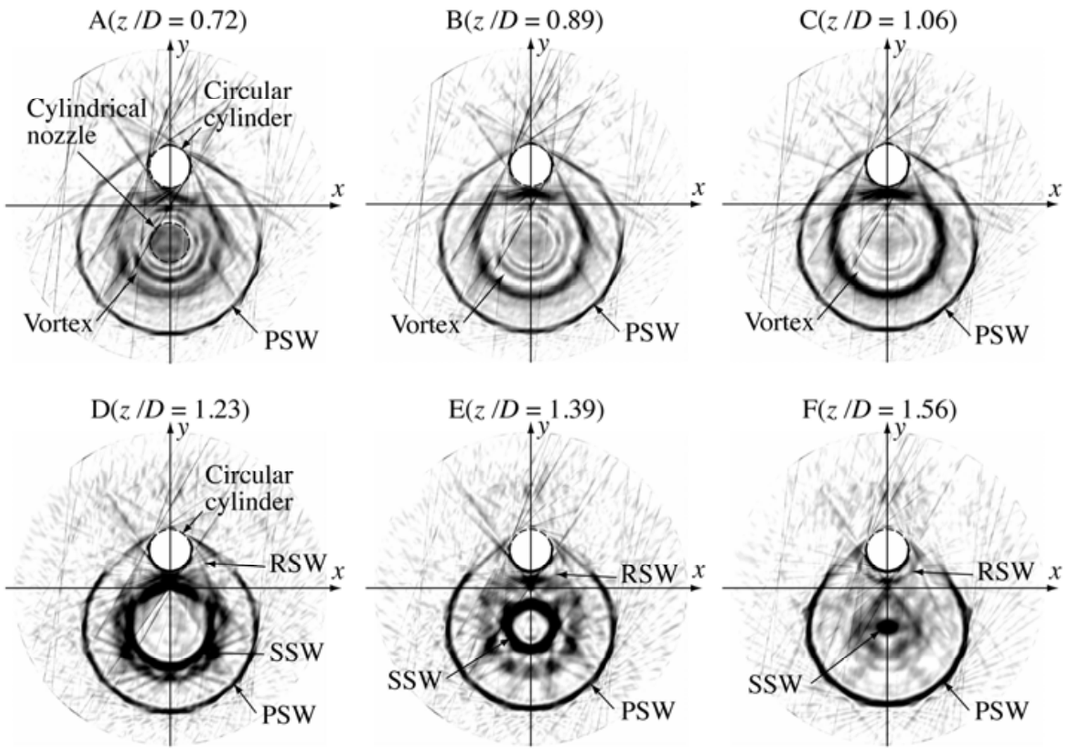

Fig. 17. Pseudo-schlieren images of density gradient ($\nabla|\rho / \rho_0|$) at *x*-*y* cross-sections.

4. Velocity measurement of shock wave in micro-scale shock tube by laser differential interferometer

Recently, the micro-shock waves have attracted attention of researchers in several fields of science. The shock wave propagating in 5.3mm inner diameter tube was measured using pressure transducers by Brouillette. As a consequence, it is experimentally clarified that the shear stress and the heat transfer between a test gas and a wall lead to significant deviations from the normal theory, especially in a small diameter shock tube (Brouillette, 2003). However, it is predicted that the pressure transducer becomes disturbance in case of using smaller tube from the difference of the representative scales between the tube and the transducer. Thus, it is very important to establish the contactless measurement method for the shock wave propagating in small diameter tubes. In this study, we measured the velocities of shock wave and the density ratios across the shock wave, generated by originally developed diaphragmless driver section, propagating in 2 and 3 mm inner diameter tubes by using laser differential interferometer.

4.1 Diaghragmless driver section with two pistons

Figure 18 shows a schematic drawing of the diahpragmless driver section, we developed; it consists of a main piston instead of a diaphragm, a sub piston, a buffer section, and a high-pressure section.

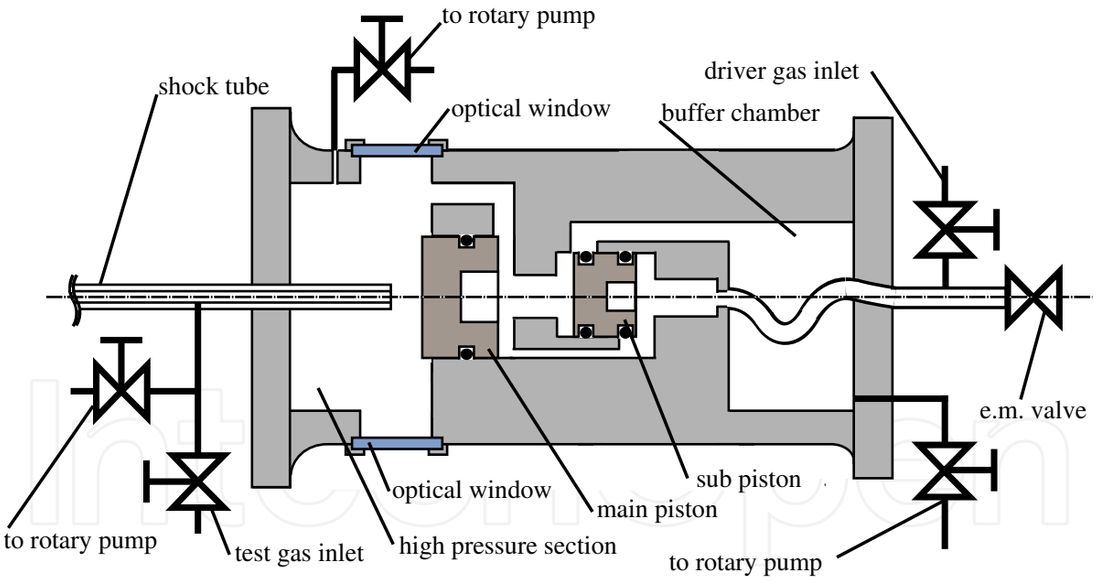

Fig. 18. Schematic drawing of the diaphragmless driver section with two pistons.

First, the buffer chamber and the region behind the sub piston are evacuated by a rotary pump, then the sub piston moves to the right side by the pressure difference. The pressure difference occurs between the high-pressure section and the region behind the main piston by the connection between the buffer chamber and the region behind the main piston after the sub piston movement. After movement of the pistons, the high-pressure section and the shock tube are evacuated by a rotary pump. The driver gas is introduced from the driver gas inlet after evacuation, and then the sub piston moves to the left side by the inlet gas

pressure. The buffer chamber and the region behind the main piston are separated by the movement of a sub piston as shown in the left side of Fig. 19. Subsequently, the main piston moves to the left side by that the driver gas flows into the region behind the main piston. The high-pressure chamber and the shock tube are also separated by movement of the main piston. Test gas is introduced from the test gas inlet after the introduction of the driver gas. The buffer chamber maintains a low-pressure state, less than 0.1 kPa. The driver gas pressures p_4 is 0.9 MPa and the test gas pressure p_1 is maintained at atmospheric pressure. The sub piston moves to the right side by controlling the electromagnetic valve, and then the main piston rapidly moves to the left side by the connection of the buffer chamber and the region behind the main piston. The shock tube and the high-pressure chamber are connected by rapid movement of a main piston as shown in the right side of Fig. 19.

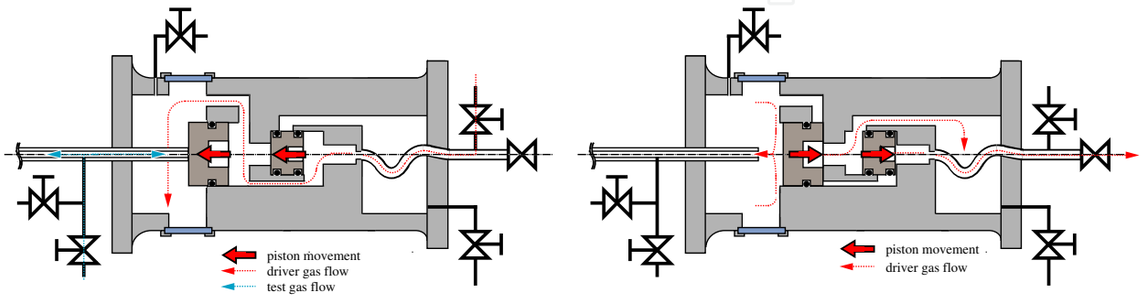

Fig. 19. Schematic drawing of the operating procedure of the diaphragmless driver section.

4.2 Measurement system

Generally the direct measurement of shock wave, by using pressure transducer is very difficult especially in the shock wave propagating in small diameter tube, caused by the difference of the representative scales between the tube and the transducer. Thus, contactless measurement by using laser interferometry is very important and useful.

4.2.1 Laser differential interferometer

Figure 20 shows the laser differential interferometer used in this experiment. The laser differential interfeormeter is the polarization phase difference interferometer by using three Wollaston prisms, developed by Smeets (Smeets, 1972; Smeets, 1977). The bright and dark, observed in the interferometric fringe, is measured by photo detectors.

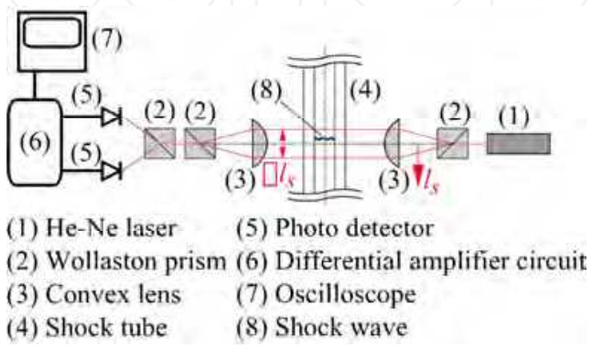

Fig. 20. Schematic drawing of the laser differential interferometer.

The laser beam from He-Ne laser head is separated into two parallel and orthogonal polarizing components after passing through the first Wollaston prism and a convex lens. The two-polarized and parallel beams are converged on the second Wollaston prism by a second convex lens after passing through the shock tube. Where, there is no interferometric fringe from the combined beams caused by the discrepancy between the polarization planes of both beams. Here, the shock wave propagates in the shock tube in a direction from the bottom to top in Fig. 20, and it is considered that the shock wave arrives between two beams. The density in front of the shock wave and the density behind the shock wave are ρ_1 and ρ_2, respectively. Two beams passing through the same optical path as light vectors are E_y and E_z, respectively as shown in Fig. 21.

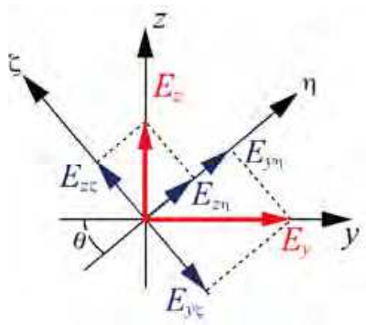

Fig. 21. Schematic drawing of the optical vectors

The light vectors E_y and E_z are denoted as follows:

$$\mathrm{E_y}=\mathrm{A_y}\cos\left(\frac{2\pi}{\lambda}\mathrm{x}\right),\quad \mathrm{E_z}=\mathrm{A_z}\cos\left\{\frac{2\pi}{\lambda}(\mathrm{x}+\Delta\phi)\right\} \tag{2}$$

Here A_y and A_z are the constants for a laser light intensity. x, λ, and Δϕ are the distance of the traveling direction of laser, the wavelength of laser, and the optical path difference between both beams, respectively. The optical path difference is occurred by the density difference across the shock wave. The third Wollaston prism should be settled as rotated 45 degrees for each polarization planes. The light vector E_y is separated into $E_{y\eta}$ and $E_{y\zeta}$, respectively. Similarly, The light vector E_z is separated into $E_{z\eta}$ and $E_{z\zeta}$, respectively. Here, η and ζ are the axes inclined 45 degree from y and z axes. After passing through the second Wollaston prism, the agreement of polarization plane causes interference at η and ζ directions, respectively. The intensities of interfering lights for η and ζ directions are denoted as follows:

$$\mathrm{I}_\eta=\left\langle\left|\mathrm{E}_{y\eta}+\mathrm{E}_{z\eta}\right|^2\right\rangle=\mathrm{A}^2\cos^2\left(\frac{\pi}{\lambda}\Delta\phi\right),\quad \mathrm{I}_\zeta=\left\langle\left|\mathrm{E}_{y\zeta}+\mathrm{E}_{z\zeta}\right|^2\right\rangle=\mathrm{A}^2\sin^2\left(\frac{\pi}{\lambda}\Delta\phi\right) \tag{3}$$

Here, $A_y = A_z = A$. The intensities of two polarized interfering beams I_η and I_ζ are converted into the voltage signals V_η and V_ζ by the photo detectors as follows:

$$\mathrm{V}_\eta=\mathrm{kI}_\eta=\mathrm{kA}^2\cos^2\left(\frac{\pi}{\lambda}\Delta\phi\right),\quad \mathrm{V}_\zeta=\mathrm{kI}_\zeta=\mathrm{kA}^2\sin^2\left(\frac{\pi}{\lambda}\Delta\phi\right) \tag{4}$$

The voltage signal V is stored to an oscilloscope. Here, k is the constant defined from the characteristics of the photo detector. The voltage signal $V = V_\eta - V_\zeta$ is amplified by the differential amplifier circuit.

$$V=\alpha\left(V_\eta - V_\zeta\right)=\alpha k A^2 \cos\left(\frac{\pi}{\lambda}\Delta\phi\right)=V_0\cos\left(\frac{\pi}{\lambda}\Delta\phi\right) \tag{5}$$

Here, α is the gain of the amplifier. Figure 22 shows the relation between the voltage signals and the optical path difference between both beams. The gain of the amplifier α is denoted as 2 in Fig. 22. Here, the refractive index of the medium is expressed as n and the length of the medium is obtained as the inner diameter of the shock tube d, the optical path difference between both beams $\Delta\phi$ is obtained as follows:

$$\Delta\phi=\left(n_2 - n_1\right)d \tag{6}$$

Here, n_2 and n_1 are the refractive index of the gas behind the shock wave and the gas in front of the shock wave, respectively. The relation between the refractive index n and the density ρ is expressed by Gladstone-Dale's formula as follows:

$$n-1=K\frac{\rho}{\rho_0} \tag{7}$$

Here, ρ_0 and K are the density at the normal condition and the non-dimensional Gladstone-Dale constant, respectively. The relation between the voltage signal V and the density difference ρ_2-ρ_1 is obtained from Eq. 5, 6 and 7 as follows:

$$V=V_0\cos\left\{\frac{2\pi dK}{\lambda\rho_0}\left(\rho_2-\rho_1\right)\right\} \tag{8}$$

Here, the voltage signal V can be linearly-approximated to ΔV at V=0 neighborhood as follows, as shown in Fig. 22:

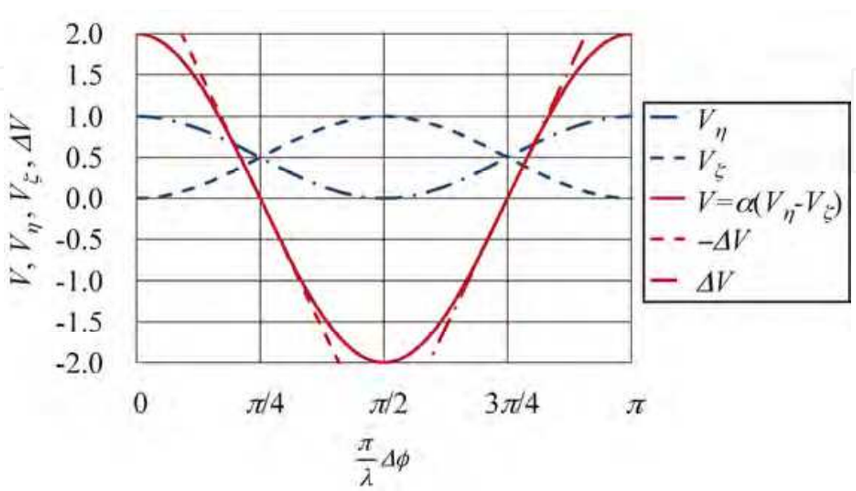

Fig. 22. The interfering signals from the laser differential interferometer.

$$\pm\Delta V=2V_0\frac{\pi dK}{\lambda\rho_0}(\rho_2-\rho_1) \tag{9}$$

Additionally, equation 9 can be rewritten by considering that the value required in this experiment is the absolute value of the voltage signal V for the density difference ρ_2-ρ_1 as follows:

$$|\pm\Delta V|=\Delta V=2V_0\frac{\pi dK}{\lambda\rho_0}(\rho_2-\rho_1) \tag{10}$$

Moreover, the above Eq. 10 can be deformed by using density ratio across the shock wave ρ_2/ρ_1 as follows:

$$\frac{\rho_2}{\rho_1}=1+\frac{\Delta V}{2V_0}=\frac{\lambda}{\pi dK}\frac{\rho_0}{\rho_1} \tag{11}$$

4.2.2 Shock wave measurement system

Figure 23 shows the shock wave measurement system used in this experiment. The glass tube, connected to the high pressure section, has the length l = 1000 mm. The position of laser differential interferometer ls is changed from 200 to 800 mm. The inner diameter of the tube d is used as 2 and 3 mm in this experiment. The pressure transducer is settled at the end of the tube to detect the reflected shock wave. The signals obtained from the interferometer and the pressure transducer are stored to an oscilloscope. The initial pressure ratio p_4/p_1 maintains constant as 9, in driven pressure p_1 = 0.1 MPa. The driver and driven gases are helium and air, respectively.

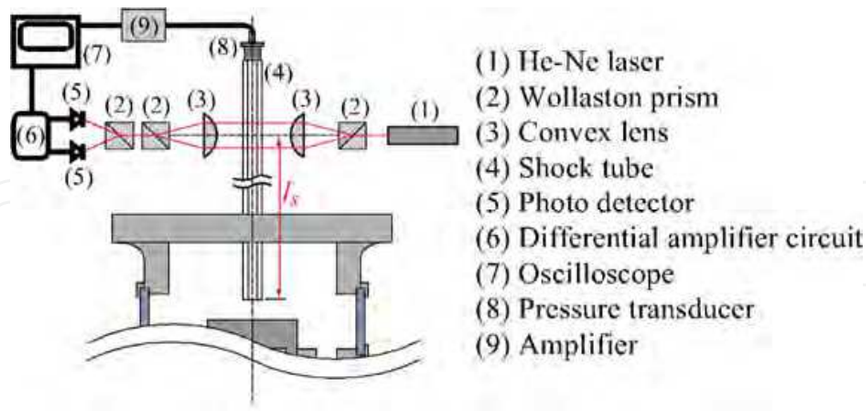

Fig. 23. The interfering signals from the laser differential interferometer.

4.3 Results and discussion

The interferometric signal of the shock wave, generated by using the diaphragmless driver section as mentioned above, propagating in the small diameter tubes is obtained from the laser differential interferometer.

4.3.1 Shock wave detection by the interferometer

Figure 24 shows the time variation of typical signal trace from the interferometer. The horizontal and vertical axes indicate the time and the voltage. The signal rising and decay in Fig. 24 show that the shock wave passes through the first beam and the second beam of the interferometer. The signal is obtained at l_s=800mm in d=2mm tube. The Mach number of shock wave M_s can be calculated by using the following equation;

$$M_s = \frac{\Delta l_s}{\Delta \tau \cdot a_1} \tag{12}$$

Here, Δls is the distance of the two beams of the interferometer, τ is the time difference between the signal rising and decay as shown in Fig. 24, and a_1 is the sound velocity of the driven gas. The Mach number is obtained as 1.53 in this case by calculating from Eq. 12.

4.3.2 Density ratio across the shock wave ρ_2/ρ_1

The density ratio across the shock wave ρ_2/ρ_1 can be calculated from Eq. 11 by using measured ΔV in Fig. 24. Figure 25 shows the relation between the density ratio across the shock wave and the Mach number. The horizontal and the vertical axes indicate the Mach number Ms and the density ratio across the shock wave ρ_2/ρ_1. The black line shows the theoretical value obtained from the following;

$$\frac{\rho_2}{\rho_1} = \frac{(\gamma_1+1)M_s^2}{(\gamma_1-1)M_s^2+2} \tag{13}$$

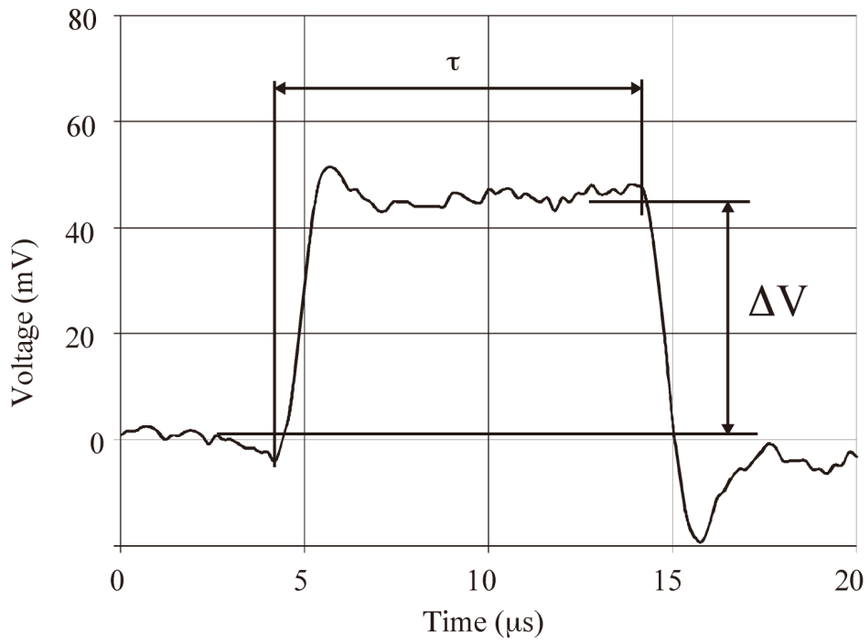

Fig. 24. The interfering signals from the laser differential interferometer.

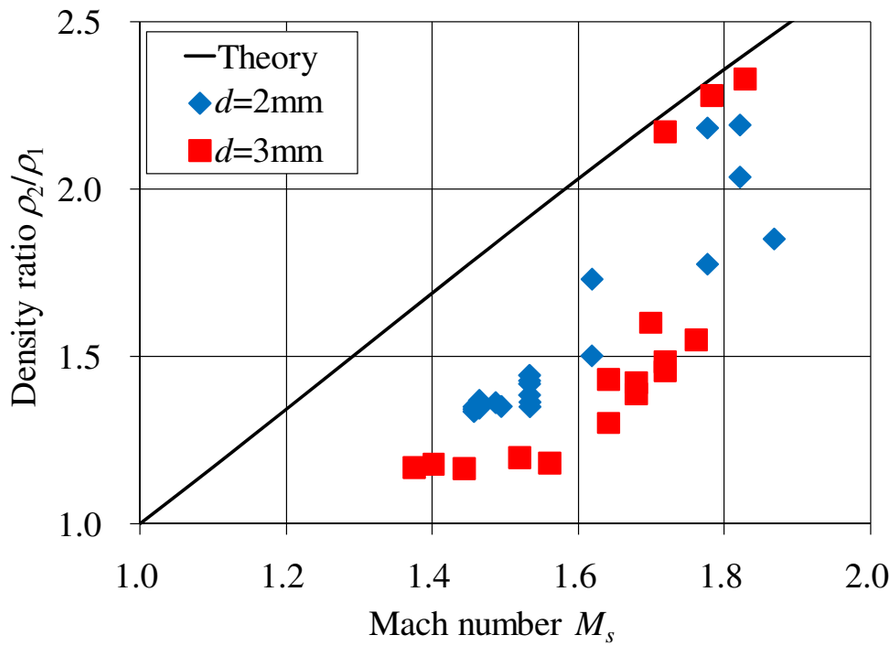

Fig. 25. Relation between ρ_2/ρ_1 and M_s.

The measured density ratio is lower than the theory. It is considered that the Gladston-Dale constant at the normal condition is used for the calculation, nevertheless the temperature behind the shock wave becomes higher. Additionally, the influence of the inner diameter of the shock tube d can be seen slightly.

5. Conclusion

This chapter described two topics related to interferometric measurement in shock tube experiment. LICT technique was applied to the measurement of high-speed, unsteady and 3D flow field induced by discharging shock waves, and laser differential interferometer was applied to velocity and density measurement in micro-scale shock tube.

For LICT measurement, 3D flow phenomena behind discharging shock wave from two parallel and circular nozzles were captured in detail. Various phenomena were clarified - shock-shock interaction, shock-vortex interaction, SSW, CS1, CS2, …etc. LICT measurement was also applied to flow field around a circular cylinder to aim at extending the tomographic measurement to more general case. Density distribution was reconstructed from incomplete projection data containing blanked part by ART algorithm. Three-dimensional flow phenomena can be captured from resultant images. However

some improvements in reconstruction will be necessary to clarify complex flow phenomena.

For velocity measurement of shock wave in micro-scale shock tube, we measured the velocities of the shock wave and the density ratios across the shock wave propagating in the small diameter tubes, generated by the diaphragmless driver section, by using laser differential interferometer. From our results the following points can be concluded. Firstly, the relation between the Mach number and the density ratio across the shock wave is obtained. The measured density ratio is lower than the theory. It is considered that the Gladstone-Dale constant at the normal condition is used for the calculation, nevertheless the temperature behind the shock wave becomes higher. Additionally, the influence of the inner diameter of the shock tube d can be seen slightly. Secondly the detailed experiments are required to estimate the influence of the shock wave attenuation by using longer shock tube.

6. Acknowledgment

Authors greatly appreciate Hiroki Honma of Professor Emeritus of Chiba University and Professor Walter Garen of Hochschule Emden/Leer, University of Applied Sciences for their valuable advice and discussion.

7. References

Brouillette, M. (2003). Shock waves at microscales, *Shock waves,* Vol.13, No.1, (April 2003), pp. 3-12, DOI 10.1007/s00193-003-0191-4.

Honma, H., Ishihara, M., Yoshimura, T., Maeno, K. and Morioka, T. (2003a), Interferometric CT measurement of three-dimensional flow phenomena on shock waves and vortices discharged from open ends, *Shock Waves* (2003a), 13, pp.179-190.

Honma, H., Maeno, K., Morioka, T. and Kaneta, T. (2003b), Some topics on three-dimensional features of shock waves and vortices discharged from open ends, *Proc. of the 5th International Workshop on Shock/Vortex Interaction* Hosted by National Cheng Kung University, The Kaohsiung Grand Hotel Kaohsiung, October 27-31.

Kak A. C., Slaney M. (1988), Principles of Computerized Tomographic Imaging, *IEEE*, New York.

Maeno, K., Kaneta, T., Yoshimura, T., Morioka, T. and Honma, H. (2005), Pseudo-schlieren CT measurement of three-dimensional flow phenomena on shock waves and vortices discharged from open ends, *Shock Waves*, Vol.14, No.4, pp.239-249.

Ota, M., Koga, T. and Maeno, K. (2005), Interferometric CT Measurement and Novel Expression Method of Discharged Flow Field with Unsteady Shock Waves, *Japanese Journal of Applied Physics*, Vol. 44, No. 42 pp. L1293-1294.

Ota M., Koga, T. and Maeno, K. (2006), Laser interferometric CT measurement of the unsteady super sonic shock-vortex flow field dischargeing from two parallel and cylindrical nozzles, *Measurement Science and Technology*, Vol. 17, pp. 2066-2071.

Shepp, A. L. and Logan, F. B. (1974), The Fourier Reconstruction of a Head Section, *IEEE Trans. Nucl, Sci.*, Ns-21, pp.21-43.

Smeets, G. (1972). Laser interferometer for high sensitivity measurements on transient phase objects, *IEEE transactions on Aerospace and Electronic Systems,* Vol.AES-8, No.2, (March 1972), pp. 186-190, DOI 10.1109/TAES.1972.309488.

Smeets, G. (1977). Flow diagnostics by laser interferometry, *IEEE transactions on Aerospace and Electronic Systems,* Vol.AES-13, No.2, (March 1977), pp. 82-89, DOI 10.1109/TAES.1977.308441.

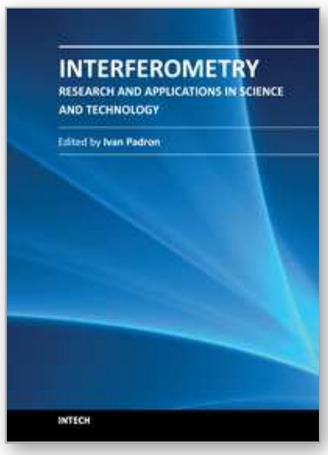

Interferometry - Research and Applications in Science and Technology

Edited by Dr Ivan Padron

ISBN 978-953-51-0403-2
Hard cover, 462 pages
Publisher InTech
Published online 21, March, 2012
Published in print edition March, 2012

This book provides the most recent studies on interferometry and its applications in science and technology. It is an outline of theoretical and experimental aspects of interferometry and their applications. The book is divided in two sections. The first one is an overview of different interferometry techniques and their general applications, while the second section is devoted to more specific interferometry applications comprising from interferometry for magnetic fusion plasmas to interferometry in wireless networks. The book is an excellent reference of current interferometry applications in science and technology. It offers the opportunity to increase our knowledge about interferometry and encourage researchers in development of new applications.

InTech Europe
University Campus STeP Ri
Slavka Krautzeka 83/A
51000 Rijeka, Croatia
Phone: +385 (51) 770 447
Fax: +385 (51) 686 166
www.intechopen.com

InTech China
Unit 405, Office Block, Hotel Equatorial Shanghai
No.65, Yan An Road (West), Shanghai, 200040, China
中国上海市延安西路65号上海国际贵都大饭店办公楼405单元
Phone: +86-21-62489820
Fax: +86-21-62489821

IntechOpen